RESEARCH ARTICLE



Laser Machined Fiber-Based Microprobe: Application in Microscale Electroporation

Jongwoon Kim¹ · Yajun Zhao² · Shuo Yang¹ · Ziang Feng¹ · Anbo Wang¹ · Rafael V. Davalos² · Xiaoting Jia¹

Received: 30 October 2021 / Accepted: 1 February 2022 © Donghua University, Shanghai, China 2022

Abstract

Microscale electroporation devices are mostly restricted to in vitro experiments (i.e., microchannel and microcapillary). Novel fiber-based microprobes enable in vivo microscale electroporation and arbitrarily select the cell groups of interest to electroporate. We developed a flexible, fiber-based microscale electroporation device through a thermal drawing process and femtosecond laser micromachining techniques. The fiber consists of four copper electrodes (80 μ m), one microfluidic channel (30 μ m), and has an overall diameter of 400 μ m. The dimensions of the exposed electrodes and channel were customizable through a delicate femtosecond laser setup. The feasibility of the fiber probe was validated through numerical simulations and in vitro experiments. Successful reversible and irreversible microscale electroporation was observed in a 3D collagen scaffold (seeded with U251 human glioma cells) using fluorescent staining. The ablation regions were estimated by performing the covariance error ellipse method and compared with the numerical simulations. The computational and experimental results of the working fiber-based microprobe suggest the feasibility of in vivo microscale electroporation in space-sensitive areas, such as the deep brain.

 $\textbf{Keywords} \ \ \text{Fiber probe} \cdot \text{Polymer} \cdot \text{Micromachine} \cdot \text{Irreversible electroporation} \cdot \text{Reversible electroporation} \cdot \text{Microscale electroporation}$

Introduction

Electroporation is a biophysical phenomenon where short (microseconds) electrical pulses, which induce high electric fields (thousands of V/cm), are used to introduce nanoscale defects in the cell membrane [1–3]. In regard to the applied pulse parameters, there are two modes of electroporation: reversible electroporation (RE) and irreversible electroporation (IRE). In the case of RE, the nanoscale defects increase the membrane permeability, allowing exogenous materials (i.e., DNA, protein, or large molecules) to be transferred

Jongwoon Kim and Yajun Zhao contributed equally to the work.

Rafael V. Davalos davalos@vt.edu

Published online: 23 March 2022

- Bradley Department of Electrical and Computer Engineering, Virginia Tech, Blacksburg, VA 24060, USA
- Department of Biomedical Engineering and Mechanics, Virginia Tech, Blacksburg, VA 24061, USA

into the cell [4–7]. The defects in the membrane can recover after the treatment, thereby maintaining high cell viability. RE drug delivery enables a lower, nontoxic concentration to be administered compared to conventional drug delivery systems [7]. For example, electrochemotherapy (ECT) is a branch of RE, where chemotherapeutics, such as bleomycin or cisplatin, are injected with a low concentration, to control the side effects of the drugs [5, 7, 8]. Another active RE research is in the DNA, RNA, and protein transfections of cells [5]. Compared to the previous method of viral-mediated gene delivery, RE is less expensive and more efficient in performing transfection [9, 10]. During an IRE treatment, higher magnitude electric fields excessively increases the permeability of the cell, leading to disturbance in the cellular homeostasis and cell death [11–15]. Traditionally, radiofrequency ablation [16], microwave ablation [17], and cryoablation [18] have been used to indiscriminately destroy undesired tissues in the body. IRE has some key advantages over these traditional methods: reduced treatment time, absence of the heat-sink effect, sharp ablation margins, and tissue selectivity [19]. Due to these advantages, IRE was transferred into the clinical trials for prostate cancer treatment in



2010 [20]. Recently, it has gained significant traction for the treatment of locally advanced pancreatic cancer as well as for liver and renal tumors. Although IRE has its advantages, the treatment volume is relatively small, and the procedure is relatively complex, involving the precise placement of a multitude of electrodes. Furthermore, due to nerve excitation during the pulse, a neuroblocker and cardiac synchronization need to be employed. Typically, four electrodes are needed for applications involving tumor ablation. The designs of new and less invasive probes [21, 22] have been proposed to alleviate these issues ranging in applications from cancer therapy to cardiac ablation.

In recent decades, scientists have studied the two modalities of electroporation in vitro and in vivo, resulting in relatively standardized protocols for the procedures [23]. Lately, both single-cell and microscale electroporation have been investigated for several purposes: higher cell viability and transfection rate, faster optimization of DNA or RNA transfection procedures, smaller volumes of samples, experiments with rare and expensive drugs, and cell selectivity [24–26]. Future works in the ablation of epilepsy and/or seizure focal points require sharp microscale ablation zones and cell selectivity [26]. Currently, the two main types of microscale electroporation devices are microcapillary [27–29] and microchannel [30-34] based devices. Microcapillarybased devices contain and electroporate the samples in the disposable reaction chambers (usually in pipettes) [35]. Microchannel-based devices manipulate the location of the samples through fluidic pumps and microchannel geometries [36]. However, these two types are not adaptable for in vivo experimental environments [26]. Recently, a glass fiber microprobe has been developed for microscale electroporation of arbitrarily selected groups, proposing the possibility of a simplified in vivo experimentation [37].

In vivo transfection of mice brain through electroporation has been studied [38-41]. Yet, many of the in vivo microscale electroporation devices are restricted to the use of pipettes with microelectrodes, which have disadvantages of bulky setups. Fiber-based probes have advantages in the scalability (thousands of devices with one thermal draw) and the consistency of device parameters (electrode separation distance) compared to the traditional in vivo microscale electroporation devices (pipettes with microelectrodes). The probes are also minimally invasive, requiring only a microscale burr hole for intracranial insertion. Deep brain regions (i.e., hippocampus, hypothalamus, amygdala, etc.) may be electroporated to eliminate or transfect desired neurons with minimal damage along the electrode insertion track. The hippocampi of rodents are roughly 20–30 mm³ and the identified layers within hippocampi, such as Dentate gyrus or CA3, are in several mm³ ranges [42, 43]. Currently, electrical (relatively low voltage compared with electroporation), chemical, and optical stimulations are the main sources of neuron manipulation used to understand the brain circuitries. For example, picosecond electrical pulses (500 ps, 10 kV/cm) were recently reported to suppress action potentials in hippocampal CA1 [44]. Pulsed electric fields elicit transient blood–brain barrier (BBB) disruption (up to 72 h) at relatively low electric fields (~100 V/cm) [45, 46]. The electric fields generated using these minimally invasive fiber-based probes lend this approach as suitable for inducing neurological phenomenon with minimal damage to intact tissue. With microscale electroporation as an additional tool to manipulate neurons, further advancements in understanding the neuronal circuitries may be possible.

The thermal drawing process (TDP), traditionally used to fabricate the optical glass fibers [47], is an emerging platform for developing multimaterial fiber-based micro-devices [48–59]. The method is highly versatile, enabling the assemblage of various functional materials in a complex crosssectional design [48, 55, 59]. The unique cross-sectional architecture leads to new innovations in fiber-based microdevices and advanced textiles for sensing, actuating, biomedical applications, and energy harvesting. From a single inexpensive preform, fibers of hundreds of meters in length are produced, thus reducing the cost and the time of the fabrication [48, 59]. Recently, a new class of multifunctional neural probe has been developed using this method, enabling simultaneous electrical recording, drug delivery, and optical and electrical stimulation in vivo [54, 55, 57]. Information, such as temperature, can be stored and processed in our daily clothing that has digital electronics embedded fibers woven in [56]. Flexible and disposable fiber has recently been designed to sense the microfluidic activities, such as the presence or the flow rate of a fluid [58]. The microfiber probes fabricated with the TDP method show promising prospects in biomedical applications. Currently, the functions of the flexible fiber-based neural probes are mostly realized locally at the tip.

We developed a new polymer fiber-based microprobe using the scalable thermal drawing process, enabling localized microscale electroporation and drug delivery at the center of the electroporation region. We exposed the electrodes and the microfluidic channel at various locations along the fiber length using a femtosecond laser micromachining technique. With two phases (source and sink) fabricated into a single fiber, pulses could be delivered with one insertion, reducing the complexity in electrode placements. The size of the microscale electroporation is customizable by adjusting the spacing between the electrode exposures and the pulse parameters. To demonstrate the two modes of electroporation, we delivered electrical pulses to a 3D collagen hydrogel scaffold in which human glioma cells (U251) were seeded. Then, RE or IRE area was determined by fluorescent staining. Numerical simulation was performed to estimate the electric field distribution in the scaffold and



determine the electric field thresholds of IRE. Our data suggest that the newly developed class of fiber-based microscale electroporation devices has the potential in conducting in vivo microscale ablation/ transfection experiments where the traditional microchannel and microcapillary-based devices had difficulties.

Material and Method

Preform Fabrication and Thermal Drawing Parameters

The thermal drawing process is a versatile fabrication method that allows thermoplastics (such as elastomers, acrylic, polypropylene, polyvinylidene fluoride, polycarbonate, polysulfone, polyetherimide, etc.) to be pulled into a fiber, maintaining the cross-sectional features. Before the preform fabrication, polycarbonate (PC) rods, tubes (McMaster-Carr), and films (Laminated Plastics) were baked in a vacuum oven at 80-90 °C for at least one week. This process ensured that no water molecules were left inside the material. For the fiber without a microfluidic channel, 4 square grooves, perpendicular to one another, were milled from a PC rod with a diameter of 2.5 cm. The side of the square grooves was 0.625 cm. The Teflon rods with a diameter of 0.625 cm were inserted into the square grooves. Then, the intermediate preform was rolled with thin PC films. The thickness of the preform after the roll was 3.125 cm. The preform was consolidated in a vacuum oven at 190 °C for 10 min on four different sides. The four Teflon rods were taken out of the preform after the consolidation. The purpose of the Teflon rods was to minimize the deformation of the square grooves during consolidation. For the fiber with a microfluidic channel, the dimensions and the steps are identical after the PC tube fabrication. A PC tube is consolidated by rolling the PC films on a Teflon rod with a diameter of 0.625 cm. The diameter of the PC rod was 2.5 cm. The next steps follow the previous preform fabrication steps.

The preform was mounted into the furnace with three temperature zones. The four copper wire spools were each mounted on a ball bearing near the top of the preform, and the wires were fed through the four hollow channels in the preform (Convergence Drawing). Another way of obtaining metal-embedded fibers is through the traditional drawing method, where low-melting temperature metals, such as BiSn, are embedded in the preform. The temperatures used during the fiber drawing were 150 °C (top), 280 °C (middle), and 110 °C (bottom). The feeding speed of the preform was set to 2 mm/min. The diameter of the fiber was controlled by varying the drawing speed, which was tuned in the range between 0.3 and 4 m/min. In order for copper wires (80 µm) to be properly inscribed in the square grooves,

the diameter of the preform had to be reduced by 62.5 folds; the aimed diameter of the fiber was $400 \, \mu m$. Fibers with a diameter larger than $400 \, \mu m$ might not hold the electrodes in place, while fibers with a diameter smaller than $400 \, \mu m$ will have a deformed cross-section, possibly clogging the microfluidic channel.

Femtosecond Laser Micromachining Setup

A regenerative Ti: Sapphire femtosecond laser with the emission wavelength of 800 nm and ~ 100 fs pulse width was used in the fabrication (Coherent Libra Series). The laser emits a collimated Gaussian beam with a beam waist of 3 mm. A half-wave plate and a linear polarizer were implemented to control both the power and polarization of the light. In this fabrication, no apparent polarization dependence was observed. Then, the light was focused onto the fiber surface through a 10× dry objective (Nikon, NA: 0.25). The same objective was also used to implement an inverted reflected light microscopy, which was used to monitor the micromachining process in real-time. The reason for an inverted design, instead of an upright design, was to reduce re-deposition during the laser micromachining process. The pulse energy used in the fabrication was 0.6 and 1 μJ, respectively, and the repetition rate was 100 Hz, which was selected to maintain reasonable machining efficiency while minimizing the thermal effect. The excessive thermal effect would damage the surrounding region of the targeted position. In order to accommodate the non-flat surface of the fibers, we used a custom-built system equipped with a rotational stage along the fiber axis to precisely position the interested area towards the laser pulses.

The smallest feature size of the femtosecond laser micromachining is tunable, depending on the numerical aperture (NA) of the objective lens. In this work, we used a 0.25 NA objective lens which has a smallest feature size of around 10 μm . The choice of this value is to balance the processing time and the details of our windows, which is around hundreds of micrometers. We have previously achieved a 1 μm feature size on polymer materials with a 0.75 NA objective lens.

The fiber was mounted on a customized holder, which was further mounted on an assembled 4-axis computer-controlled motion stage, including linear translations in x, y, z directions (ASI MS-2000, ASI LS-50, and Newport UTM50CC) and rotations around fiber axial direction (Thorlabs PRM1Z8). Necessary manual kinetic mounts were also implemented to ensure the parallelism between the fiber and the stage's translation axis. The micro-hole was machined via the line-by-line and layer-by-layer method. The size of the machined mark for a single pulse was roughly 10 µm in diameter, and thus the center-to-center distance between



lines was set at 5 μ m to ensure sufficient overlap. The scanning speed of each line was 150 μ m/s.

Cell Culture

Malignant glioma cells, U251 (Sigma Aldrich, 09063001), were cultured in Dulbecco's Modified Eagle's Medium (DMEM) supplemented with a 10% fetal bovine serum (Sigma-Aldrich, St. Louis, MO, USA) and a 1% penicillin/streptomycin (Invitrogen, Carlsbad, CA, USA). The cells were incubated at 5% CO₂ and 37°C. The media was changed every other day, and the cells were passaged at around 90% confluence.

Collagen Scaffold Preparation

3D printed wells were designed as the treatment chambers to carry the hydrogel and the fiber microprobe. The inner diameter of the chamber was 1 cm. To insert the fiber probe into the chamber, we created $\Phi = 1$ mm holes at the wells' front and rear sides. These holes were 0.5 mm higher than the bottom of the chamber. After the insertion of the microprobe, each hole was fixed with medical epoxy. The customdesigned chambers were sterilized by UV light before seeding the collagen with cells. For the 3D scaffold, 10×DMEM (10% total volume, Sigma Aldrich) and 1 N NaOH (about 2% collagen volume, Sigma Aldrich) were added to the collagen to mediate its pH neutralization. U251 cell suspension and its media were added to obtain the final concentration of the collagen to be 5 mg/mL and the cell concentration to be 2×10^6 cells/mL. To ensure immersion of the fiber probe in the thin hydrogel layer, we transferred the cell-seeded collagen hydrogel to each well to achieve a final thickness of 1.5 mm. Then, the chambers were placed in a $\Phi = 10$ cm Petri dish. The Petri dish was left in the incubator for 30 min, where the collagen polymerized. 600 µL cell culture media was added to each well after the collagen polymerization, and the collagen scaffolds were incubated for 24 h before electroporation treatments.

Electroporation Set-up

To deliver the electrical pulses to the scaffold, we connected the two copper electrodes from the immerged microprobe to the pulse generator (BTX, Harvard Apparatus, Holliston, MA, USA). Both test and control groups were connected to the generator. However, the treatment pulses were only applied to the test groups. An oscilloscope (DPO2002B, Tektronix Inc., Beaverton, Oregon), combined with a high voltage probe (Enhancer 3000, BTX, Holliston, MA) and current sensor (3927, Pearson Electronics, Palo Alto, CA) was used to record the applied voltage and the response current.



To observe the reversible electroporation effect, we dyed the cells in the scaffold before the treatment. We observed the electroporation effect immediately after the pulsing. The media in each well was aspirated and replaced with 300 μL dye solution, containing 1 μM YO-PRO-1 (Thermo Fisher Scientific) and 2.5 $\mu g/mL$ Calcein red AM (Thermo Fisher Scientific). The petri dish containing the wells was wrapped in aluminum foil to avoid any exposure to light. The scaffolds with the dyes were placed in the incubator for 30 min before treatment. The microprobes with the microfluidic channel windows were used for the RE test. After the treatment, every scaffold was imaged using a Zeiss LSM880 (Carl Zeiss Microscopy, NY) laser scanning confocal microscope.

For irreversible electroporation, the scaffolds were treated before staining. The cell culture media was aspirated from each well before treatment. We used the microprobes without any microfluidic channels for IRE treatment. After treatment, $600 \, \mu L$ media was added to each well and incubated for 24 h before staining. The media was aspirated then replaced by 300 μL of 2.5 μg/mL Calcein green AM and 15 μg/mL PI dissolved in phosphate-buffered saline (PBS) to dye the live and dead cells, respectively. The aluminum foil-wrapped petri dish was used to place the wells to avoid light, and the dyed samples were incubated for 30 min. After the staining solution had been aspirated and the samples were washed twice by PBS, the wells were imaged using the confocal microscope. To examine the ablation area at various planes, we used the Z-stack scanning with a step size of 5 μm to capture the images from bottom to top. Zeiss ZEN 3.0 (Carl Zeiss Microscopy, NY) was used to control the confocal microscope and export the images for the following analysis. The images were processed using a custom-written Matlab script to determine the ablation area and volume.

Numerical Model

A cylinder with a diameter of 1 cm and a thickness of 1.5 mm was built in a commercial finite element package (COMSOL Multiphysics, v5.6, Stockholm, Sweden) to represent the scaffold. A model of the fiber probe, four copper wires enclosed by a polycarbonate cylinder, was placed in the middle of the scaffold representation. The two neighboring wires were exposed to the scaffold in a $40\times200~\mu m$ window. The center-to-center distance of the windows was 0.95 mm. All these dimensions were the averaged measurement results from the fabricated fibers. The aimed dimension of the window and the center-to-center distance were $40\times150~\mu m$ and 1 mm. The electric field distribution in the hydrogel was solved by the Laplace Eq. (1), and the Joule heating during the treatment was considered to



estimate the temperature rise during the treatment. The temperature was calculated by the heat transfer Eq. (2):

$$-\nabla^2(\varphi) = 0 \tag{1}$$

$$-\rho c_p \frac{\partial T}{\partial t} = \nabla \cdot (k \nabla T) + Q_J \tag{2}$$

where φ is the electric potential in the domain. ρ is the tissue density, c_p is the specific heat capacity of the tissue, k is the thermal conductivity of the tissue. Q_I is the Joule heating.

The electric and thermal properties of collagen were obtained from Arena et al. [52], as shown in Table 1. The electrode (Copper) property is from the COMOL Material Library. The pulse parameters for the simulation were 200 pulses with an amplitude of 500 V, pulse width of 100 μ s, and a repetition rate of 1 Hz, which were employed in the IRE experiment in the study.

The electric field threshold of the irreversible electroporation was obtained by matching the volume wrapped in the electric field isosurface to the measured ablation volume.

Electroporation Volume Estimation

With the specific electrode configuration, the ablation region for each slice was elliptical. Thus, we implemented the covariance error ellipse method to estimate the ablation area of each slice to determine the volume of the ablation. The covariance error ellipse method calculates a confidence interval dependent contour of the bivariate Gaussian distribution estimated with the sample data [61]. The magnitude and the angle of the ellipse axes depend on the covariance matrix of the sample data. The computed eigenvalues represent the absolute spread of the sample data, while the eigenvector represents the direction of the spread. The equations for the error ellipse and the orientation of the ellipse are:

$$\left(\frac{x}{\lambda_1}\right)^2 + \left(\frac{y}{\lambda_2}\right)^2 = s \tag{3}$$

$$\theta = \tan^{-1} \left(\frac{v_1(y)}{v_1(x)} \right) \tag{4}$$

Table 1 The physical properties used in the simulation

Parameter	Electrode	Collagen scaffold
k (W/m K)	400	0.6
c (J/kg K)	385	4181.8
ρ (kg/m ³)	8940	997.8
σ (S/m)	5.998×10^7	1.2

where λ_1 and λ_2 are the largest and the smallest eigenvalue of the covariance matrix. s is the scale of the ellipse and is the Chi-Square likelihood of the confidence level and the degrees of freedom (i.e., 90% confidence level with 2 degrees of freedom corresponds to s=4.602). v_1 is the eigenvector of the largest eigenvalue. The detailed steps and derivations of the method are available in the textbook [53]. We wrote a custom Matlab script to output the areas and the images with the drawn error ellipse. Then, we estimated the volume of the ablation with the known thickness between each slice (5 μ m) and the areas.

Results and Discussions

Thermal Drawing Process

Two varieties of the fiber were fabricated using the TDP method for microscale electroporation (Fig. 1). Due to the high electrical voltage during the electroporation, we utilized polycarbonate as the insulating medium of the fiber device for its high dielectric breakdown voltage (200 kV/ cm). Thin films of PC were baked in an oven vacuum for 7 days to remove the water inside. In this way, undesirable, random pores will be avoided in the fiber during the thermal drawing process. As shown in Fig. 1a, a preform was fabricated by rolling, consolidating, and milling. After each rolling of PC films, the intermediate preform was put in a vacuum oven to remove the air in between the film layers and therefore consolidated. The preform was mounted in the 3-layered temperature controllable furnace for the fiber productions (Fig. 1b). The four spools of copper wire fed the wires from the top of the preform to the bottom of the fiber. The TDP process was closely monitored through the temperature sensors, the strain sensor, and laser micrometer. We controlled the diameter of the fiber by adjusting the temperature of the furnace and/or the drawing speed of the fiber. The diameter of the fiber was reduced by 40-60 folds while maintaining the cross-sectional features of the preform.

In a typical draw, we can obtain a fiber of several hundred meters (Fig. 1c). In Fig. 1d, the flexibility of the fiber is demonstrated by wrapping the fiber around a conventional pen. The cross-sections of the two varieties of the fiber are shown in Fig. 1e and f, respectively. The diameters of the fibers and the copper wires are $398 \pm 17~\mu m$ and $80~\mu m$. The diameter of the microfluidics channel in the second design is $27 \pm 8~\mu m$. The edges of the rectangular grooves are maintained in the fiber. By these copper electrodes alone, microscale electroporation of arbitrarily selected cell groups can be achieved at the tip of the fiber, similar to the previously reported glass fiber probe. However, there is a limitation in the size of the electroporation due to the fixed distance of the two electrodes at the tip. New sets of preform fabrication



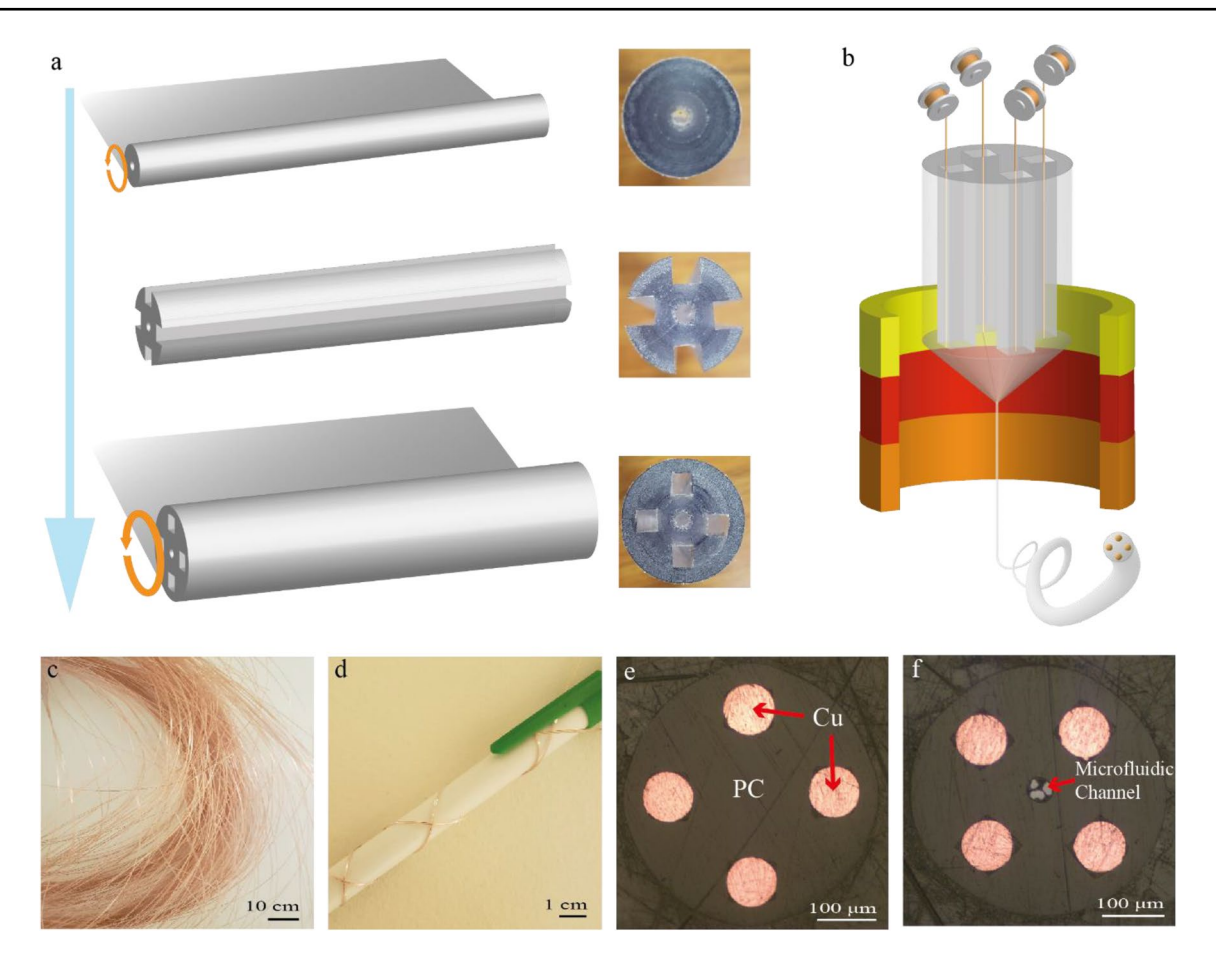


Fig. 1 Thermal Drawing process of the fiber-based microprobe. **a** A representative preform fabrication process and the corresponding preform cross-sections. **b** A schematic of the thermal drawing process of the fiber. **c** A single thermally drawn fiber with the length of over

300 m. **d** A demonstration of the flexibility of the polymer fiber. \mathbf{e} , \mathbf{f} A cross-section of the fiber with four copper electrodes with and without microfluidic channel

and thermal drawing need to take place for various distances between electrodes. We overcame this challenge by implementing a femtosecond micromachining technique along the fiber length to enable distributed functional sites, eliminating the labor demanded to fabricate various electrode distances for different sizes of microscale electroporation.

Electrode Exposure and Microfluidic Windows Through Femtosecond Laser Micromachining

To expose the electrodes and the microfluidic channel along the fiber length, we adapted a custom femtosecond laser setup. The schematic and the picture of the laser setup are shown in Fig. 2a. The system is fully controlled with custom LabView panels, enabling precise manipulations of the fiber in x, y, z, and rotational directions. We investigated the optimal laser parameters and the fiber orientations for the various sizes and depths of the exposed electrodes and microfluidic channels. In Fig. 2b, c, we show the before and after femtosecond micromachining technique along the fiber

length. We observed black dust or residues of PC around the exposure, similar to the residual melt from cutting PC using a CO₂ laser [54]. The depth required to expose the electrode was 30-40 µm; this depth is directly proportional to the preform dimension. We experimentally determined that 0.6 µJ for the pulse energy cut deep enough to expose copper electrodes. The quality controls of the exposed electrode were conducted in the following manner. We covered the tip of the fiber probe with a medical epoxy. Then, we measured the impedance of the exposed electrode using a potentiostat (Interface 1010E, Gamry Instruments) in phosphate-buffered saline (PBS, Thermo Fisher). We observed a high impedance when the micromachining did not expose copper electrodes because PC and epoxy are electrically insulating material. Statistically, roughly 5% of the exposed electrodes with the pulse energy of 0.6 µJ were still covered with PC. This is due to the slight irregular thickness of the electrode covering the PC layer. We utilized Zygo Newview 8200 with a 10× Mirau objective to capture the 3-dimensional features of the exposed electrode (Fig. 2e). As shown in SI(video),



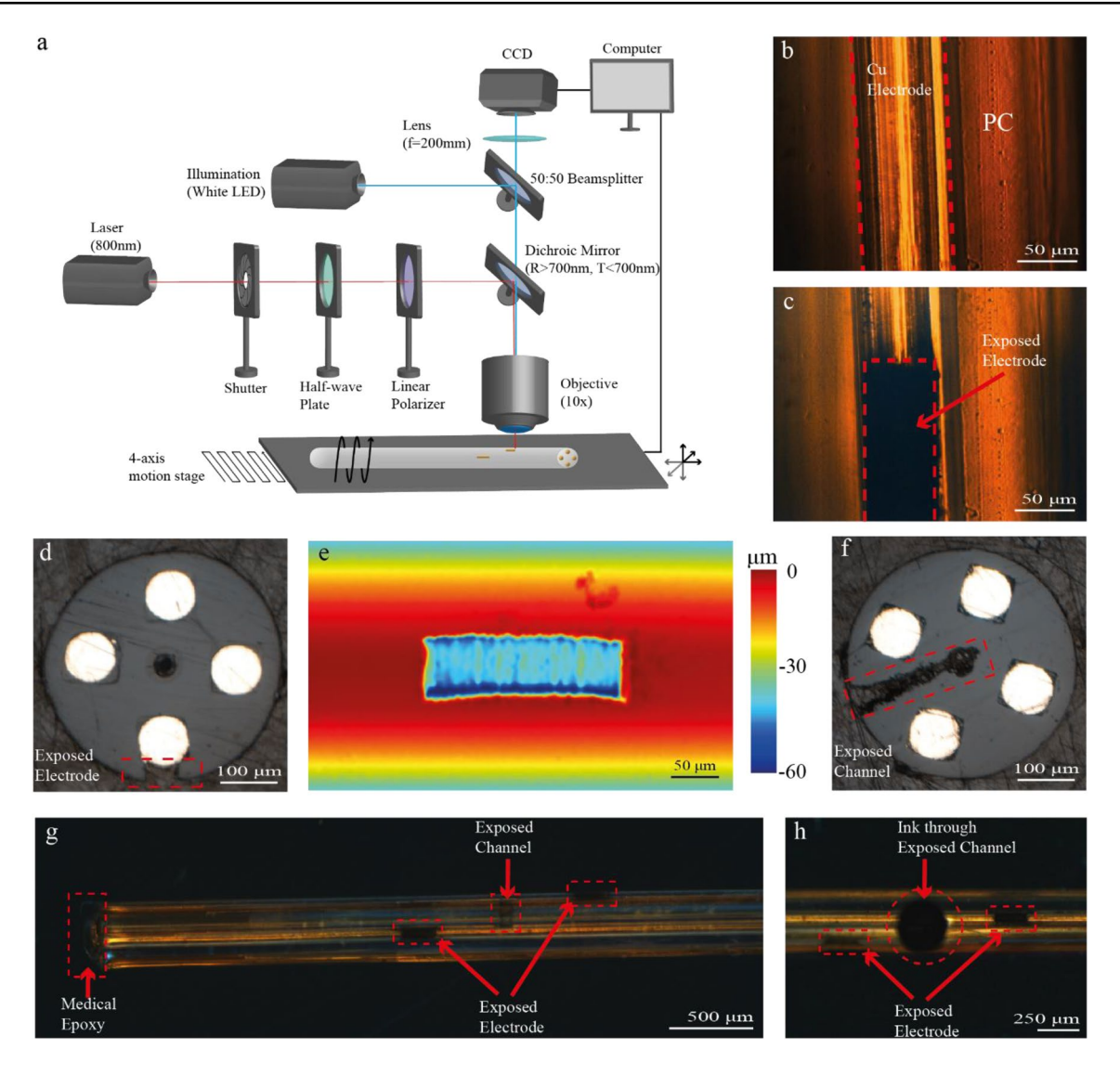


Fig. 2 Femtosecond laser micromachining techniques along the fiber length. **a** A schematic of custom femtosecond laser setup to expose electrodes and the microfluidic channel. **b, c** An image taken by the CCD from the laser setup before and after the micromachining. Black dust and PC residues are visible after the laser micromachining. **d** A cross-section of the fiber with an exposed electrode. **e** A profiling image to show the 3-dimensional features of the exposed electrode. There is a 50×200 μm rectangular exposure with a depth of

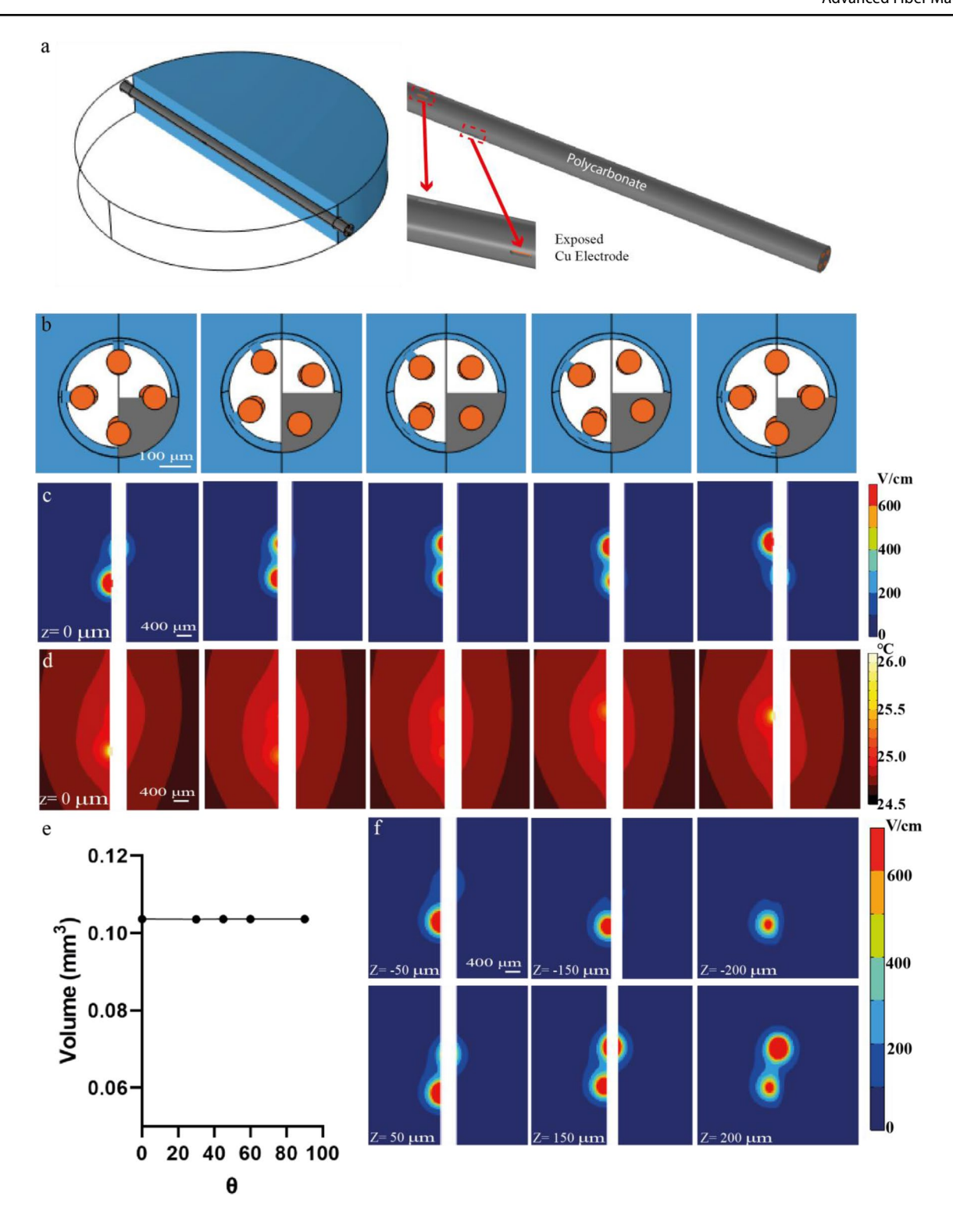
40–60 μ m. **f** A cross-section of the fiber with an exposed microfluidic window. The dimension of the rectangular exposure is $30 \times 100~\mu$ m with a depth of ~200 μ m. **g** An image of the fiber-based microprobe for microscale electroporation. The tip of the fiber is mechanically and electrically insulated with medical epoxy. The two electrodes are exposed for electroporation and an exposed channel for drug delivery. **h** A demonstration of the drug delivery using ink

the laser cuts layer by layer from the top to the bottom of the electrode exposure.

We grooved a 30×100 µm rectangular window, which connects the microfluidic channel to the outside. The cross-section of the exposure is shown in Fig. 2f. To cut narrow and deep into the microfluidic channel, we employed 1 µJ for the pulse energy and rectangular micromachining at 6 different depths. Two criteria of the orientation had to be met in order to have a successful microfluidic window. The laser had to point into the center of the microfluidic channel, and the angular orientation

of the fiber had to be closely manipulated such that the two electrodes are equidistant from the laser location. In Fig. 3g, we present our flexible, fiber-based, microscale electroporation probe. The tip of the fiber is mechanically and electrically insulated with a medical epoxy, allowing no drug to be delivered and/ or any microscale electroporation at the tip. For this specific fiber probe, we exposed two 50 by 200 µm electrode windows, roughly 1 mm apart. 400 µm below the first electrode exposure, we fabricated a 30 by 100 µm microfluidic window. By exposing different dimensions and changing the distance





between the electrode exposures using the femtosecond laser micromachining, we can achieve various microscale electroporation sizes. Additionally, there is no limit to the number of exposures on the same electrode, possibly introducing multiple microscale electroporation along the fiber length. The two unused electrodes may be exposed

to a more dynamic electric field (microscale electroporation shapes) or measurements (impedance changes). In Fig. 2h and SI, we demonstrated local drug delivery near the microfluidic channel by injecting a purple dye. The video (SI) displays no leakage of dye at the tip or along the fiber length.



◄Fig. 3 Numerical Simulation of the Electroporation Effects Using the Fiber-based Microprobe. a The geometry of the 3D scaffold (only half presented here) and the fiber-based microprobe. Enlarged detail of the fiber and the exposed copper wire on the right model. b The schematic of the fiber probes placed with different angles to the vertical directions (from left to right, $\theta = 0^{\circ}$, 30° , 45° , 60° , and 90°). Only a quarter of the polycarbonate in the fiber is presented to better visualize the exposed places of the fiber. The blue substance outside the fiber is the 3D hydrogel scaffold. The exposure is visible between the 3D hydrogel scaffold and the copper wire. c, d The electric field and temperature distributions at the middle plane of the 3D scaffold for different angles (from left to right, $\theta = 0^{\circ}$, 30° , 45° , 60° , and 90°). Pulse parameters used were: 200, 500 V,100 µs, 1 Hz pulses. e Ablation volume for the fiber probes with different angles to the wells $(\theta = 0^{\circ}, 30^{\circ}, 45^{\circ}, 60^{\circ}, \text{ and } 90^{\circ} \text{ as shown in } \mathbf{b})$. The irreversible electroporation threshold was 450 V/cm. f The electric field distributions at different planes when $\theta = 0$. Z=200 and - 200 μ m are the planes tangent to the upper or nether side of the fiber. Pulse parameters used were: 200, 500 V,100 μs, 1 Hz pulses

Numerical Simulation of Microscale Electroporation

The geometry of the setup is shown in Fig. 3a. Only half of the collagen scaffold is presented to display the position of the fiber in the hydrogel. The exterior boundaries are electrically and thermally insolated. Two exposures of the fiber electrode are set to source ($\varphi = V$) and sink ($\varphi = 0$) phases, respectively. Figure 3b shows the angular orientation of the fiber probe with respect to the scaffold. To easily visualize the positions of the two exposed parts, we only show a quarter of polycarbonate (grey part) in Fig. 3b. In the actual fiber device, the polycarbonate fills the whole void as insulating and support layers of the four electrodes. The two small windows that connect the collagen and the electrode represents the exposed electrodes. There was a concern in the distribution of the electric field and the electroporation region due to the thinness of the hydrogel and the orientation of our fiber probe. Depending on the orientation of the probe, the relative positions of the top and bottom boundaries of the hydrogel to the exposed electrodes could affect the electric field distribution. We investigated the electric field and the temperature distribution with respect to the angular orientation of the fiber probe. The angle between the upper exposure and the vertical plane, θ , is investigated at 0° , 30° , 45° , 60° , and 90° .

Figure 3c and d show the respective electric field and temperature distribution at the center plane of the collagen layer for various θ . At the center plane of the scaffold, the electric field and the temperature distributions differ with respect to the probe angular orientation. Since the electric field distribution directly influences the electroporation region, the orientation of the fiber probe (exposed electrodes) has to be consistent for each well, or else the ablation region at each depth for different wells will not agree. The temperature distribution results show that the maximum temperature rises only by 2 $^{\circ}$ C for the irreversible electroporation parameters.

Hence, the ablated area formed in hydrogel experiments is mainly caused by irreversible electroporation rather than thermal damage.

The ablation volumes for different rotations of the fibers are given in Fig. 3e. The irreversible threshold, 450 V/cm, was obtained by matching the calculated ablation volume to the volume surrounded by the electric field isosurface and comparable to the previously reported values[52, 60]. We observed no large fluctuations in the final ablation volumes at various angular orientations of the probe. The electric field distribution at different layers for $\theta = 0^{\circ}$ is shown in Fig. 3f. Due to the configuration of the two exposed electrodes, the ablation areas at different layers are inconsistent. This makes it difficult to determine the electric field by matching the area between the simulation and the numerical results; thus, we used the ablated volume to calculate the electric field threshold.

In Vitro Microscale Electroporation

Electroporation experiments were performed in a 3D hydrogel scaffold in which malignant glioma cells U251 were seeded to demonstrate the feasibility of the fiber electrodes in electroporation application. The experiment setup is shown in Fig. 4a. Treatment pulses were generated by the pulse generator and recorded through an oscilloscope. Although the simulation showed no ablation volume changes with respect to the angular orientations of the probe, we consistently placed the fiber probe with $\theta = 0^{\circ}$ to obtain consistent images. Each fiber was immersed in the hydrogel scaffold with a thickness of 1.5 mm. After the study of the control group, we concluded that the 1.5 mm thickness of the hydrogel in the scaffold did not have a large effect on the cell viability. A typical pulse waveform is shown in Fig. 4b. The amplitude of the clean voltage waveform was 500 V. We observed a consistent spike at the onset of the current waveform, followed by some noise throughout the pulse on-time. This could be caused by the relatively low current value.

First, we employed this setup to test the reversible electroporation effect. Pulse parameters were set to 100 pulses with a pulse width of 100 μs , a pulse amplitude of 300 V, and a repetition rate of 1 Hz. Before treatment, the 3D scaffolds with cells were dyed by YO-PRO-1 and Calcein red AM. Treatment pulses were applied 30 min after the staining. Each well was imaged immediately after the treatment. The unaffected cells presented red fluorescence, indicating live cells with an intact membrane structure. The dissipation of red fluorescence or the expression of green fluorescence is an index of electroporation of membranes, as shown in Fig. 4c. The dark band beside the electroporation zone is the position of the fiber. This is a pilot study to validate that the fiber electrodes proposed here can create effective reversible electroporation.



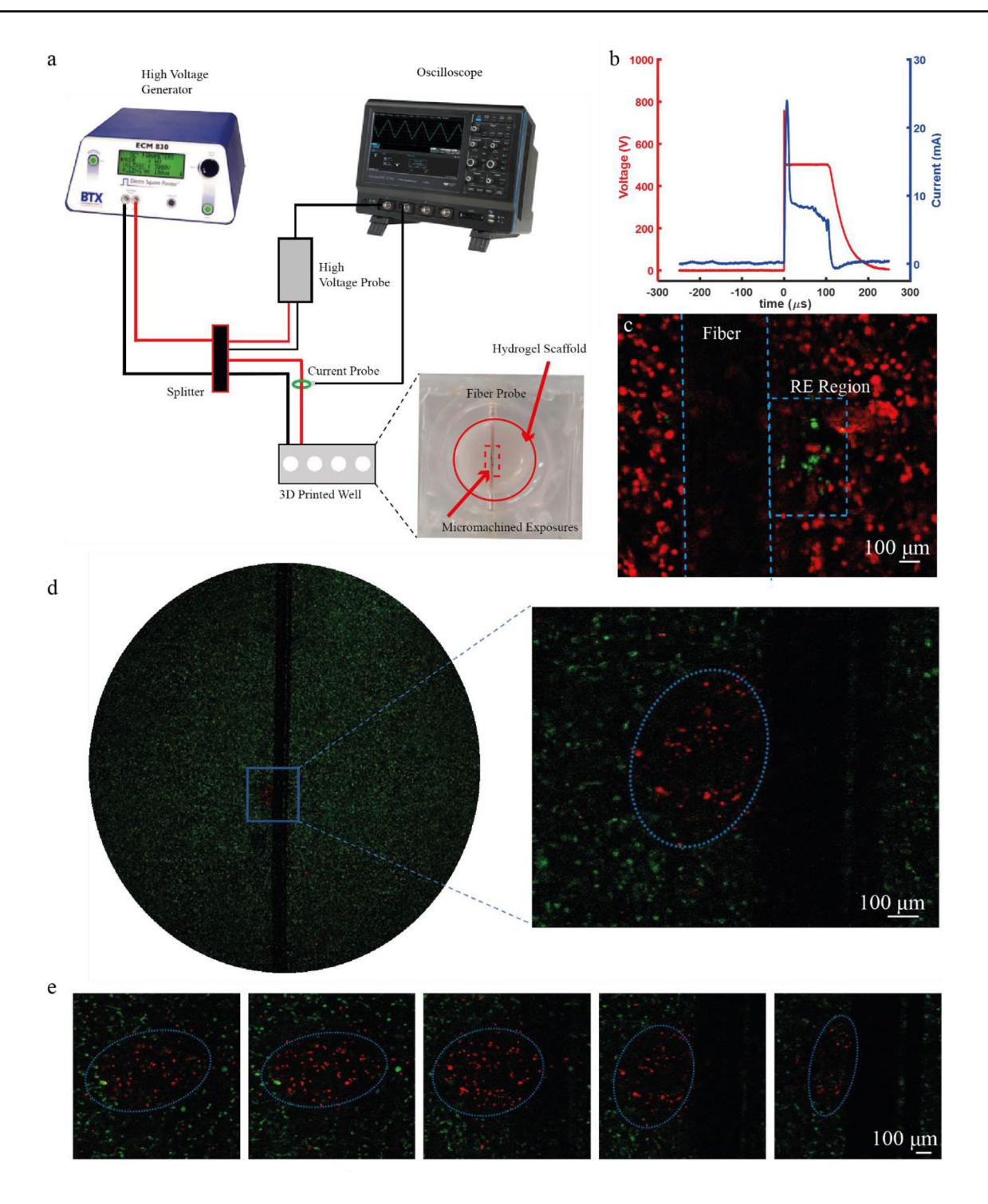


Fig. 4 Electroporation Experiments Using the Fiber-based Microprobe in 3D Collagen Scaffold with Malignant Glioma Cells U251. **a** The experimental setup. **b** A typical voltage (500 V, 100 μs) and current waveforms. **c** A representative image of the reversible electroporation region indicated by the YO-PRO-1 (green) surrounded by live cells indicated by Calcein red AM (red). **d** A representative image of irreversible electroporation area indicated by the Propidium Iodide

(red) surrounded by live cells indicated by Calcein green AM (green). The dark band beside the ablation area is the position of fiber. ${\bf e}$ A representative image of irreversible electroporation area at various depths. The blue dashed ellipses layered on the ablation regions are the estimated boundary calculated with the covariance error ellipse method



To further validate the stability at a higher pulse dose for irreversible electroporation, we increased the pulse parameters to 200, 100 µs, 500 V, 1 Hz pulses. The hydrogel scaffolds were dyed with Propidium Iodide (PI) and Calcein green AM 24 h after pulsing to assess the irreversible electroporation effects. Green fluorescence (Calcein green) indicates live cells, while red fluorescence (PI) stands for the dead cells. Figure 4d is a typical image showing the ablation results at a certain plane. The dark band across the well is the position of the fiber. The ablated area with red fluorescence beside the fiber can be identified. For the traditional two-needle electrode configuration, the ablation regions at different planes are similar. However, the ablation regions of the fiber probe at different planes cannot be comparable due to the different electrode configurations. A z-stack scanning (with a step of 5 µm) of the ablated area was used to obtain the ablation area at different planes, as shown in Fig. 4e. A time-lapsed video of the z-plane scan is included in the supplementary information to aid the visualization of the 3d ablation volume. As to the simulation results in Fig. 3f, it was challenging to find the exact z-plane of ablation from the fluorescent images due to the small ablation size and the uneven distribution of the cells. However, we observed that the experimental results (Fig. 3f) match the simulation results (Fig. 4e) at multiple z-planes (e.g. from $Z = 150 \mu m$ to $Z = 200 \mu m$, at $Z = -50 \mu m$, and at $Z = 50 \mu m$). These results demonstrated the feasibility of producing microscale irreversible electroporation using the developed fiber electrodes.

We implemented the covariance error ellipse method to estimate the area of ablation at each plane. The ablation volume was estimated by integrating the elliptical area over the height through which we did the z-stack scanning. A custom Matlab script was written to input the images and output the equation and the area of the ellipses. The output covariance error ellipses were layered on top of Fig. 4d, e. The average area of the specific ablated region at each plane was $0.241 \pm 0.05 \text{ mm}^2$, and the volume was 0.1099mm^3 . The area of each plane can differ drastically with respect to the angular orientation of the fiber probe.

Customization of the Electrode Exposures

A key advantage of our fiber microprobe compared with the previously reported glass fiber probe is the customization of the electrode exposure sizes and the separation distance between the electrode exposures. The exposure size and the separation distance directly contribute to the electric field; thereby, the customization enables the manipulation of the microscale electroporation size and shape. We exposed the fiber electrodes in four unique designs to demonstrate the customization flexibility, shown in Fig. 5. The first design consists of two side-by-side electrode exposures. The second design has two exposures on the same electrode while only one exposure on the adjacent electrode. The dimension of the exposures is $50 \times 100 \,\mu\text{m}$. In the third design, we changed the dimension of the exposure from $50 \times 100 \,\mu\text{m}$ to $50 \times 400 \,\mu\text{m}$. Lastly, we exposed all four electrodes, keeping

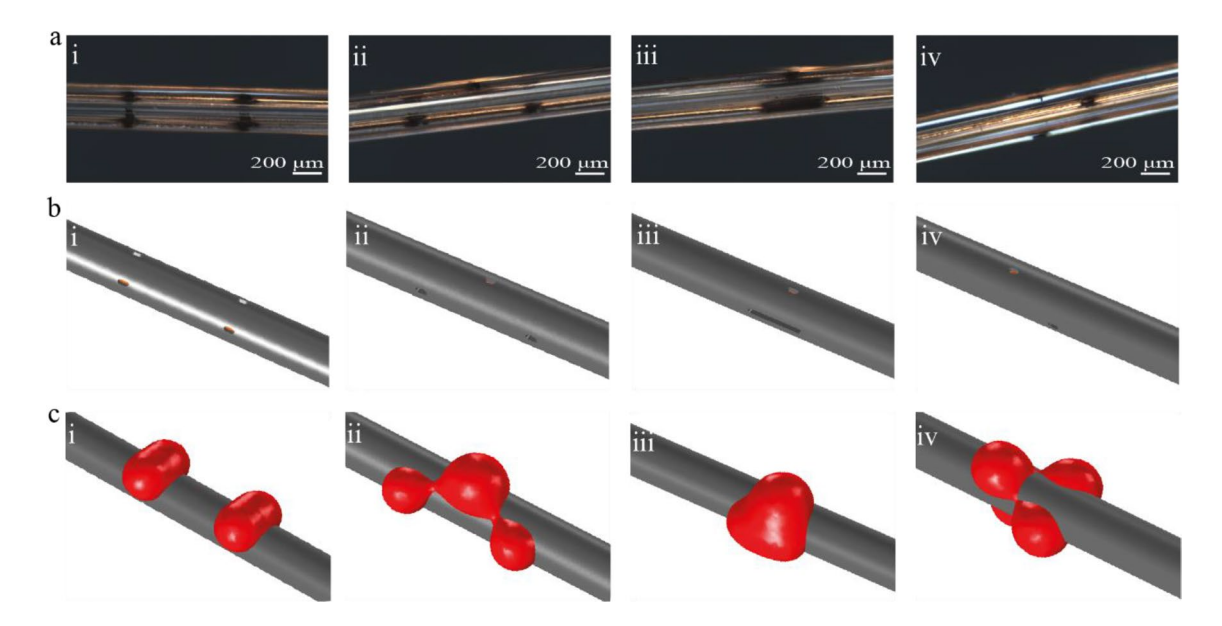


Fig. 5 Ablation area control by customizing electrode exposures. **a** Femtosecond machined exposures along the fiber length. **i** Two side-by-side electrode exposures along the fiber length. **ii** Two exposures on one electrode and one exposure on the adjacent electrode. **iii** Side-by-side electrode exposures with different sizes. **iv** Four exposures

from each four electrodes. b The corresponding simulation setup for each electrode exposure configuration. c The corresponding simulated ablation volumes for microscale irreversible electroporation applications



the parallel electrodes on the same plane. In Fig. 5b, the corresponding simulation setup of the designs are presented. The hydrogel experiments were not further conducted because we expect the numerical simulations to reflect the experimental ablation shape, as discussed in the previous section.

With the same parameters from the hydrogel experiment, we simulated and calculated the ablation volume for each design (Fig. 5c). The calculated ablation volumes from the first to the fourth design were 0.097, 0.106, 0.069, 0.090 mm³.

Conclusions

Here, we present a novel device for microscale electroporation of cells through developing a flexible, polymer, fiberbased microprobe for both in vitro and in vivo experiments. The electrodes and the microfluidic channel were exposed along the fiber length through a custom-built femtosecond laser micromachining setup. The different electroporation sizes and shapes were realizable through customizing the electrode exposure sizes and distances between the exposures. We computed the numerical simulations to visualize the electric fields and the temperature distributions of the functioning microprobe at different angles. To validate the feasibility of the proposed fiber electrode in electroporation, we designed a 3D hydrogel scaffold, where the malignant glioma cells (U251) were seeded, and the fiber probe was placed in the middle. The two modes of the microscale electroporation were conducted, varying the number and voltage of electrical pulses. The reversible and irreversible electroporation areas were observed by fluorescent staining. The ablation volumes were estimated by integrating the area, estimated with the covariance error ellipse method, over the height. The in vitro experiments and the numerical simulations demonstrate the microscale electroporation through our fiber microprobe. Compared with the current microscale electroporation devices, the fiber-based microprobes enable arbitrary control of cell selectivity and more systematic in vivo experiments, such as unrevealing the mysteries in the deep intercortical circuitries.

Acknowledgements X.J. gratefully acknowledges funding support from US National Science Foundation (ECCS-1847436) and US National Institutes of Health (R01 NS123069-01 and R21 EY033080-01). R.D. gratefully acknowledges funding support from National Institutes of Health (R01CA213423).

Declarations

Conflict of interest The authors state that there are no conflicts of interest to disclose.



References

- Jordan CA, Neumann E, Sowers AE. Electroporation and electrofusion in cell biology. Berlin: Springer Science & Business Media; 2013.
- Tsong TY. Electroporation of cell membranes. Electroporation and electrofusion in cell biology. Berlin: Springer; 1989. p. 149.
- 3. Weaver JC, Chizmadzhev YA. Theory of electroporation: a review. *Bioelectrochem Bioenerg* **1996**;41:135.
- Neumann E, Schaefer-Ridder M, Wang Y, Hofschneider P. Gene transfer into mouse lyoma cells by electroporation in high electric fields. *EMBO J* 1982;1:841.
- Luo D, Saltzman WM. Synthetic DNA delivery systems. Nat Biotechnol 2000:18:33.
- Luxembourg A, Evans CF, Hannaman D. Electroporation-based DNA immunisation: translation to the clinic. *Expert Opin Biol Ther* 2007;7:1647.
- 7. Mir LM, Orlowski S, Belehradek J, Paoletti C. Electrochemotherapy potentiation of antitumour effect of bleomycin by local electric pulses. *Eur J Cancer Clin Oncol* **1991**;27:68.
- Sersa G, Cemazar M, Miklavcic FD. Antitumor effectiveness of electrochemotherapy with cis-diamminedichloroplatinum (II) in mice. *Cancer Res* 1995;55:3450–5.
- Kotnik T, Rems L, Tarek M, Miklavčič D. Membrane electroporation and electropermeabilization: mechanisms and models. *Annu Rev Biophys* 2019;48:63.
- Ginn SL, Alexander IE, Edelstein ML, Abedi MR, Wixon J. Gene therapy clinical trials worldwide to 2012—an update. J Gene Med 2013:15:65.
- Adam R, Hagopian EJ, Linhares M, Krissat J, Savier E, Azoulay D, Kunstlinger F, Castaing D, Bismuth H. A comparison of percutaneous cryosurgery and percutaneous radiofrequency for unresectable hepatic malignancies. *Arch Surg* 2002;137:1332.
- Davalos RV, Mir L, Rubinsky B. Tissue ablation with irreversible electroporation. Ann Biomed Eng 2005;33:223.
- 13. Edd JF, Horowitz L, Davalos RV, Mir LM, Rubinsky B. In vivo results of a new focal tissue ablation technique: irreversible electroporation. *IEEE Trans Biomed Eng* **2006**;53:1409.
- 14. Goldberg SN, Hahn PF, Tanabe KK, Mueller PR, Schima W, Athanasoulis CA, Compton CC, Solbiati L, Gazelle GS. Percutaneous radiofrequency tissue ablation: does perfusion-mediated tissue cooling limit coagulation necrosis? *J Vasc Interv Radiol* 1998;9:101.
- Miller L, Leor J, Rubinsky B. Cancer cells ablation with irreversible electroporation. *Technol Cancer Res Treat* 2005;4:699.
- Mirza AN, Fornage BD, Sneige N, Kuerer HM, Newman LA, Ames FC, Singletary SE. Radiofrequency ablation of solid tumors. Cancer J (Sudbury, Mass) 2001;7:95.
- 17. Simon CJ, Dupuy DE, Mayo-Smith WW. Microwave ablation: principles and applications. *Radiographics* **2005**;25:S69.
- Friedman PL, Wang P, Cravalho EG. Cryoablation catheter and method of performing cryoablation. Google Patents. 1992.
- Jiang C, Davalos RV, Bischof JC. A review of basic to clinical studies of irreversible electroporation therapy. *IEEE Trans Biomed Eng* 2015;62:4.
- Onik G, Rubinsky B. Irreversible electroporation: first patient experience focal therapy of prostate cancer. Berlin, Heidelberg: Springer; 2010.
- Hsiao CY, Huang KW. Irreversible electroporation: a novel ultrasound-guided modality for non-thermal tumor ablation. J Med Ultrasound. 2017;2017:5.
- Zhao Y, Mckillop IH, Davalos RV. Modeling of a single bipolar electrode with tines for irreversible electroporation delivery. Comput Biol Med 2021;2021:104870.

- Aycock KN, Davalos RV. Irreversible electroporation: background, theory, and review of recent developments in clinical oncology. *Bioelectricity* 2019;1:214.
- Fox M, Esveld D, Valero A, Luttge R, Mastwijk H, Bartels P, van den Berg A, Boom R. Electroporation of cells in microfluidic devices: a review. *Anal Bioanal Chem* 2006;385:474.
- Kim JA, Cho K, Shin MS, Lee WG, Jung N, Chung C, Chang JK. A novel electroporation method using a capillary and wire-type electrode. *Biosens Bioelectron* 2008;23:1353.
- Lee WG, Demirci U, Khademhosseini A. Microscale electroporation: challenges and perspectives for clinical applications. *Integr Biol* 2009:1:242.
- Zabzdyr JL, Lillard SJ. New approaches to single-cell analysis by capillary electrophoresis. TrAC Trends Anal Chem 2001;20:467.
- Yeung ES. Study of single cells by using capillary electrophoresis and native fluorescence detection. J Chromatogr A 1999;830:243.
- Jankowski JA, Tracht S, Sweedler JV. Assaying single cells with capillary electrophoresis. TrAC Trends Anal Chem 1995;14:170.
- Sedgwick H, Caron F, Monaghan PB, Kolch W, Cooper JM. Labon-a-chip technologies for proteomic analysis from isolated cells. *J R Soc Interface* 2008;5:S123.
- Ouyang M, Hill W, Lee JH, Hur SC. Microscale symmetrical electroporator array as a versatile molecular delivery system. *Sci Rep* 2017;7:44757.
- Kim JA, Cho K, Shin YS, Jung N, Chung C, Chang JK. A multichannel electroporation microchip for gene transfection in mammalian cells. *Biosens Bioelectron* 2007;22:3273.
- Garcia PA, Ge Z, Moran JL, Buie CR. Microfluidic screening of electric fields for electroporation. Sci Rep 2016;6:21238.
- Geng T, Zhan Y, Wang H-Y, Witting SR, Cornetta KG, Lu C. Flow-through electroporation based on constant voltage for large-volume transfection of cells. *J Control Release* 2010;144:91.
- Verpoorte E. Microfluidic chips for clinical and forensic analysis. *Electrophoresis* 2002:23:677.
- Jain T, Muthuswamy J. Bio-chip for spatially controlled transfection of nucleic acid payloads into cells in a culture. *Lab Chip* 2007;7:1004.
- Kulbacka J, Kasztelanic R, Kotulska M, Pysz D, Stępniewski G, Stępień R, Saczko J, Miklavčič D, Buczyński R. Ultrathin glass fiber microprobe for electroporation of arbitrary selected cell groups. *Bioelectrochemistry* 2020;135:107545.
- dal Maschio M, Ghezzi D, Bony G, Alabastri A, Deidda G, Brondi M, Sato SS, Zaccaria RP, Di Fabrizio E, Ratto GM, Cancedda L. High-performance and site-directed in utero electroporation by a triple-electrode probe. *Nat Commun* 2012;3:960.
- Nomura T, Nishimura Y, Gotoh H, Ono K. Rapid and efficient gene delivery into the adult mouse brain via focal electroporation. Sci Rep 2016;6:29817.
- Saito T, Nakatsuji N. Efficient gene transfer into the embryonic mouse brain using in vivo electroporation. Dev Biol 2001;240:237.
- Judkewitz B, Rizzi M, Kitamura K, Häusser M. Targeted singlecell electroporation of mammalian neurons in vivo. *Nat Protoc* 2009:4:862.
- Peirce J, Chesler E, Williams R, Lu L. Genetic architecture of the mouse hippocampus: identification of gene loci with selective regional effects. *Genes Brain Behav* 2003;2:238.
- Jacobs LF, Gaulin S, Sherry DF, Hoffman GE. Evolution of spatial cognition: sex-specific patterns of spatial behavior predict hippocampal size. *Proc Natl Acad Sci* 1990;87:6349.
- Li C, Wang S, Zhang Y, Wang E, Yao C, Mi Y. Picosecond pulse electrical field suppressing spike firing in hippocampal CA1 in rat in vivo. *Bioelectromagnetics* 2020;41:617.

- Lorenzo MF, Thomas SC, Kani Y, Hinckley J, Lee M, Adler J, Verbridge SS, Hsu F-C, Robertson JL, Davalos RV, Rossmeisl JH Jr. Temporal characterization of blood-brain barrier disruption with high-frequency electroporation. *Cancers* 1850;2019:11.
- 46. Sharabi S, Bresler Y, Ravid O, Shemesh C, Atrakchi D, Schnaider-Beeri M, Gosselet F, Dehouck L, Last D, Guez D, Daniels D, Mardor Y, Cooper I. Transient blood-brain barrier disruption is induced by low pulsed electrical fields in vitro: an analysis of permeability and trans-endothelial electric resistivity. *Drug Deliv* 2019;26:459.
- Temelkuran B, Hart SD, Benoit G, Joannopoulos JD, Fink Y. Wavelength-scalable hollow optical fibres with large photonic bandgaps for CO 2 laser transmission. *Nature* 2002;420:650.
- 48. Loke G, Yan W, Khudiyev T, Noel G, Fink Y. Recent progress and perspectives of thermally Drawn multimaterial fiber electronics. *Adv Mater* **2020**;32:1904911.
- Bayindir M, Sorin F, Abouraddy AF, Viens J, Hart SD, Joannopoulos JD, Fink Y. Metal-insulator-semiconductor optoelectronic fibres. *Nature* 2004;431:826.
- Gumennik A, Stolyarov AM, Schell BR, Hou C, Lestoquoy G, Sorin F, McDaniel W, Rose A, Joannopoulos JD, Fink Y. All-infiber chemical sensing. Adv Mater 2012;24:6005.
- Chocat N, Lestoquoy G, Wang Z, Rodgers DM, Joannopoulos JD, Fink Y. Piezoelectric fibers for conformal acoustics. *Adv Mater* 2012;24:5327.
- Khudiyev T, Clayton J, Levy E, Chocat N, Gumennik A, Stolyarov AM, Joannopoulos J, Fink Y. Electrostrictive microelectromechanical fibres and textiles. *Nat Commun* 2017;8:1435.
- Egusa S, Wang Z, Chocat N, Ruff ZM, Stolyarov AM, Shemuly D, Sorin F, Rakich PT, Joannopoulos JD, Fink Y. Multimaterial piezoelectric fibres. *Nat Mater* 2010;9:643.
- Canales A, Jia X, Froriep UP, Koppes RA, Tringides CM, Selvidge J, Lu C, Hou C, Wei L, Fink Y, Anikeeva P. Multifunctional fibers for simultaneous optical, electrical and chemical interrogation of neural circuits in vivo. *Nat Biotechnol* 2015;33:277.
- 55. Yan W, Richard I, Kurtuldu G, James ND, Schiavone G, Squair JW, Nguyen-Dang T, Das Gupta T, Qu Y, Cao JD, Ignatans R, Lacour SP, Tileli V, Courtine G, Löffler JF, Sorin F. Structured nanoscale metallic glass fibres with extreme aspect ratios. *Nat Nanotechnol* 2020:15:875.
- Loke G, Khudiyev T, Wang B, Fu S, Payra S, Shaoul Y, Fung J, Chatziveroglou I, Chou PW, Chinn I, Yan W, Gitelson-Kahn A, Joannopoulos J, Fink Y. Digital electronics in fibres enable fabricbased machine-learning inference. *Nat Commun* 2021;12:3317.
- Du M, Huang L, Zheng J, Xi Y, Dai Y, Zhang W, Yan W, Tao G, Qiu J, So KF, Ren C, Zhou S. Functional probes: flexible fiber probe for efficient neural stimulation and detection. *Adv Sci* 2020;7:2070086.
- Dong C, Page AG, Yan W, Nguyen-Dang T, Sorin F. Microstructured multimaterial fibers for microfluidic sensing. *Adv Mater Technol* 2019;4:1900417.
- Loke G, Alain J, Yan W, Khudiyev T, Noel G, Yuan G, Missakian A, Fink Y. Computing fabrics. *Matter* 2020;2:786.
- Arena CB, Szot CS, Garcia PA, Rylander MN, Davalos RV. A three-dimensional in vitro tumor platform for modeling therapeutic irreversible electroporation. *Biophys J* 2012;103:2033.
- Ghilani CD. Adjustment computations: spatial data analysis. Hoboken: Wiley; 2017.

Publisher's Note Springer Nature remains neutral with regard to jurisdictional claims in published maps and institutional affiliations.

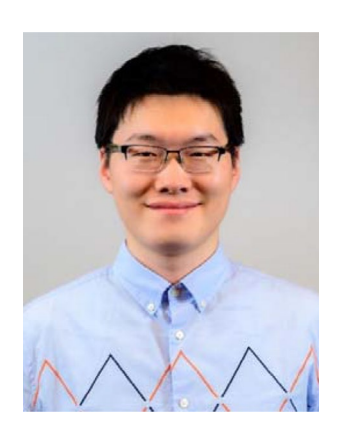




Jongwoon Kim received his B.A. degree in Physics at Ohio Wesleyan University (2015), B.S. and M.S. degree in Electrical Systems Engineering at Washington University in St. Louis (2018). He is currently a Ph. D. candidate in the Bradley Department of Electrical and Computer Engineering at Virginia Tech. His research interests include multimaterial fibers and signal processing for biomedical applications.



Yajun Zhao received the B.S. and Ph.D. degrees from Chongqing University, China, in 2013 and 2018, respectively. He worked as a postdoctoral research assistant at Virginia Tech, from 2019 to 2021. He is currently an Associate Professor with Nanjing Tech University, Nanjing, China. His research interests include pulsed power technology, high voltage discharge plasma, and their applications in biomedicine.



Shuo Yang is a postdoctoral research associate in the department of biomedical engineering in Washington University in St. Louis, St. Louis, MO, USA. He received his Ph.D. degree in Electrical Engineering from Virginia Tech, Blacksburg, VA, USA, in 2020. His research interests include photoacoustic imaging and optical sensing.



Ziang Feng is a postdoctoral research associate at Washington University in St. Louis. His research interests include multimaterial multi-functional fibers, fiber-optic sensors, and energy harvesting. He obtained his Ph.D. degree in Electrical Engineering from Virginia Tech (2020), M.Eng. in Optical Engineering and B.S. in Optical Information Science and Technology from Beijing Jiaotong University (2015 and 2012).



Anbo Wang received the doctoral degree in optics from the Dalian University of Technology, Dalian, China, in 1990. He subsequently joined the Fiber and Electro-Optics Research Center. Department of Electrical and Computer Engineering, Virginia Polytechnic Institute and State University (Virginia Tech) as a Staff Member to continue his research in fiber sensors. He was appointed as an Assistant Professor with the same Department in 1994 and was promoted to Associate Professor and then Profes-

sor in 1997 and 1999, respectively. He is the Founding Director of the Center for Photonics Technology. He is the author of 350 journal and conference papers and 25 U.S. and international patents in the field of fiber optics and sensors. Dr. Wang has supervised more than 100 graduate students and postdocs during his tenure at Virginia Tech and currently holds the Clayton Ayre Professorship. He is a SPIE Fellow.



Rafael V. Davalos is an Endowed Professor in the Virginia Tech -Wake Forest University School of Biomedical Engineering and Sciences. He is also Director of Virginia Tech's Center for Engineered Health and a Program Leader of Wake Forest's Comprehensive Cancer Center. His research interests are in microfluidics for personalized medicine and developing technologies for cancer therapy. Davalos has authored 138 peer-reviewed articles and has 37 issued patents. He has been a plenary

speaker for several prestigious venues including the International Symposium of the Bioelectrochemistry Society, the World Congress on Electroporation, and the Society of Cryobiology Annual Meeting. Davalos is an ASME and AIMBE Fellow and recipient of the 2021 ASME Van C. Mow Medal. Dr. Davalos received his bachelor's from Cornell and doctorate from Berkeley.



Xiaoting Jia is an assistant professor in the ECE department at Virginia Tech. Her research focuses on multimaterial fibers for biomedical and wearable applications. Before joining Virginia Tech, she was a postdoc associate in the Research Laboratory of Electronics at MIT. She received her Ph.D. in Materials Science and Engineering from MIT (2011), M.S. in Materials Science and Engineering from Stony Brook University (2006), and B.S. in Materials Science from Fudan University in China

(2004). She has published over 40 journal articles, with a total citation of over 14,000 times. She is a recipient of NSF CAREER award, 3 M Non-Tenured Faculty Award, ICTAS Junior Faculty Award at Virginia Tech, and the Translational Fellow at MIT.

